Reaction Chemistry & Engineering

PAPER

View Article Online
View Journal | View Issue

Cite this: *React. Chem. Eng.*, 2019, 4, 1431

Solar-driven co-thermolysis of CO_2 and H_2O promoted by *in situ* oxygen removal across a non-stoichiometric ceria membrane†

Maria Tou, [a] Jian Jin,[bc] Yong Hao,[bc] Aldo Steinfeld [a] and Ronald Michalsky *[a]

Received 28th September 2018,
Accepted 13th March 2019

DOI: 10.1039/c8re00218e

rsc.li/reaction-engineering

We report on the first ever experimental demonstration of simultaneous thermolysis of CO_2 and H_2O with *in situ* separation of fuel and oxygen in a solar-driven membrane reactor. Gaseous CO_2/H_2O mixtures at molar ratios from 3 : 4 to 2 : 1 were fed to a mixed ionic–electronic conducting non-stoichiometric ceria ($CeO_{2-\delta}$) membrane enclosed in a solar cavity receiver and exposed to simulated concentrated solar radiation of up to 4200 suns. Reaction rates were measured under isothermal and isobaric conditions in the range of 1723–1873 K and 0.2–1.7 Pa O_2, yielding a maximum combined CO and H_2 fuel production rate of 2.3 μmol cm^{-2} min^{-1} at 1873 K and 0.2 Pa O_2 at steady state, which corresponded to a conversion of reactants of 0.7%. Under all conditions tested, CO production was favored over H_2 production, as expected from theory. Experimental results followed the same trends as the thermodynamic equilibrium limits of membrane-assisted thermochemical fuel production.

Introduction

The utilization of the vast solar energy resource for electricity, heat, and fuels has become a key objective in research and development.[1] The conversion and storage of solar energy in fuels is especially appealing as a means to transition from fossil fuels to a "CO_2 economy".[2] With this, a solar refinery needs to be developed where solar energy is collected and used to convert CO_2 and H_2O to fuels by some method. Existing research spans solar-driven electrochemical, photoelectrochemical, and photocatalytic paths for direct conversion, as well as indirect routes *via* the solar thermochemical production of syngas (H_2 and CO).[3]

Solar thermochemical redox cycles utilize the entire spectrum of solar radiation concentrated to high-temperature process heat to drive the splitting of CO_2 and H_2O and produce CO and H_2 at high rates, selectivity, mass conversions, and efficiencies.[4–6] However, the temperature swing required between the redox steps induces significant material stresses and energy irreversibility, which prompted the search for alternative isothermal processes.[7–9] One promising approach is the use of a dense, ceramic, mixed ionic–electronic conducting (MIEC) membrane for the continuous separation of oxygen and fuel (H_2 and/or CO) derived from the thermolysis of CO_2 and H_2O at high temperatures, as pioneered for solar water splitting by Fletcher and co-workers.[10,11] We recently demonstrated the proof-of-concept utilization of a solar-driven membrane reactor for splitting of CO_2.[12] Other investigations of thermochemical membrane reactors, both theoretical and experimental, have also only focused on either CO_2- or H_2O-splitting.[10,13–18] This work goes further and demonstrates the feasibility of co-feeding both CO_2 and H_2O and assesses the relative favorability between the two thermolysis reactions occurring simultaneously. The desired dissociations are chemical equilibrium reactions in the gas phase described by:

$$CO_2 \leftrightarrow CO + \frac{1}{2}O_2 \quad (1)$$

$$H_2O \leftrightarrow H_2 + \frac{1}{2}O_2 \quad (2)$$

The reactions are analogous; that is, both are endothermic and thermolytic, but their reaction energetics differ. This is described by the standard Gibbs free energy changes at equilibrium ($\Delta G = 0$):

$$\Delta G_1^\circ = RT \ln\left(\frac{p_{CO} \cdot p_{O_2}^{1/2}}{p_{CO_2}} p^{\circ(-1/2)}\right) = RT \ln K_1 \quad (3)$$

[a] *Department of Mechanical and Process Engineering, ETH Zürich, 8092 Zürich, Switzerland. E-mail: michalskyr@ethz.ch*
[b] *Institute of Engineering Thermophysics, Chinese Academy of Sciences, 11 Beisihuanxi Rd., Beijing 100190, P. R. China*
[c] *University of Chinese Academy of Sciences, No.19A Yuquan Rd., Beijing 100049, P. R. China*

† Electronic supplementary information (ESI) available. See DOI: 10.1039/c8re00218e

$$\Delta G_2^\circ = RT\ln\left(\frac{p_{H_2}\cdot p_{O_2}^{1/2}}{p_{H_2O}}\,p^{\circ(-1/2)}\right) = RT\ln K_2 \quad (4)$$

where ΔG_i° is related to the equilibrium constant K_i which in turn is a function of temperature only. Fig. 1a shows $T - p_{O_2}$ equilibrium contours of the separate thermolysis of CO_2 and H_2O for various mole fractions of CO or H_2 in the product gas, respectively. For both CO_2 and H_2O thermolysis, products are favored with increasing T and decreasing p_{O_2}, *i.e.* higher mole fractions of fuel are possible towards the upper-left corner of Fig. 1a. At such high T, dissociation of CO_2 is more thermodynamically favorable than that of H_2O under equal conditions.[19,20] A decrease in p_{O_2} can be achieved without the use of high-value electrical energy by removal of O_2 utilizing a dense membrane made of an oxygen-selective MIEC material.[21] p_{O_2} is controlled to a low value on the opposite side of the membrane. For each of the separate thermolysis reactions, if $p_{O_2} \geq 1/2\ p_{CO}$ or $p_{O_2} \geq 1/2\ p_{H_2}$, the membrane provides no benefit.

The membrane reactor concept used in this work for the co-thermolysis of H_2O and CO_2 is shown schematically in Fig. 1b. CO_2 and H_2O are fed to the inner side of a capped tubular non-stoichiometric ceria membrane. Ceria has become the benchmark material for oxygen-cycling applications due to its stability and fast kinetics.[22–24] In our previous work it was also found to be an effective material for oxygen-conducting membranes.[12] The supply of concentrated solar process heat at high temperatures drives the thermolysis, producing CO, H_2, and O_2. The latter adsorbs on the inner membrane surface, dissociates, and is transported across the membrane in an ionic form along a chemical potential gradient. O^{2-} then associates into O_2 at the outer membrane surface and desorbs into an inert sweep gas contained in a shell tube. This *in situ* removal of one of the reaction products drives the reactions forward towards dissociation and avoids downstream recombination. The counter-flow configuration of the reactant and product gases favorably maximizes the gradient of p_{O_2} along the length of the membrane. By placing this reactor in a solar cavity receiver, the high-temperature heat for the reactions is provided by concentrated solar radiation incident on the shell tube.

Typical operating conditions require temperatures around 1773 K and partial pressures of O_2 down to 1 Pa. These high temperatures eliminate the need for catalysts but pose significant constraints on the construction materials which must withstand these conditions over extended periods of time. Materials must also resist thermal shock that may occur due to cooling overnight, unless the reactor is equipped with an alternative heat source such as a high-temperature thermal energy storage system.[25] A modular tubular membrane design could avoid costly maintenance by allowing for simple replacement of degraded membranes. Maintaining low partial pressures of oxygen is crucial, requiring additional energy for vacuum pumping or gas separation to regenerate the inert sweep gas (such as N_2, though here we use Ar for gas analytic considerations).[26,27] Alternatively, some studies have reported solar-driven production of pure O_2 and inert gas with low partial pressures of oxygen using thermochemical oxygen pumps driven by low-grade process heat.[27–29]

Experimental

Materials

Cerium(IV) oxide (ceria, CeO_2, powder, particle size <5 μm, 99.9% purity), poly(oxy-1,4-phenylene sulfonyl-1,4-phenylene) (PES, $(C_{12}H_8O_3S)_n$, pellets), polyvinylpyrrolidone (PVP, $(C_6H_9NO)_n$, powder, average M.W. 40 000), and 1-methyl-2-pyrrolidinone (NMP, C_5H_9NO, liquid, ≥99.0% purity) were from Sigma Aldrich. Al_2O_3 membranes (Alsint 99.7, 7 mm outer diameter (OD), 5 mm inner diameter (ID), 250 mm length) were from Intertechno-Firag AG. High-purity alumina adhesive (Aremco Ceramabond 569) and glass-filled

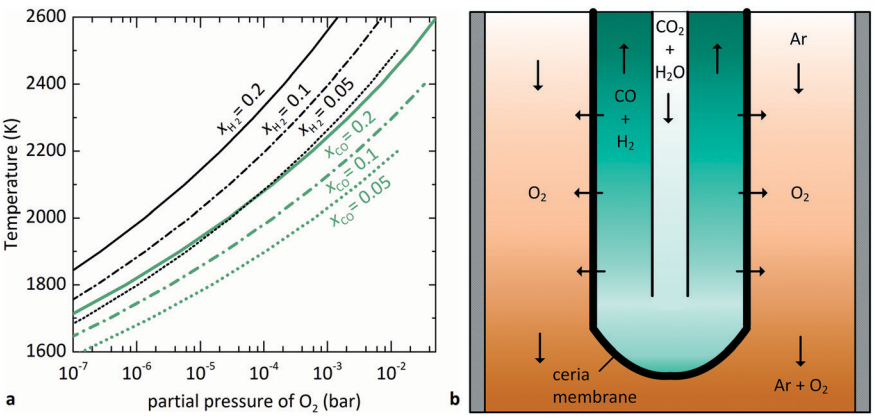

Fig. 1 (a) Equilibrium contours for separate thermolysis of CO_2 (light-colored) or H_2O (dark-colored) at 1 bar total pressure as a function of T and p_{O_2} (according to eqn (3) and (4)) for various mole fractions of CO or H_2, respectively. Contours extend until p_{CO} or $p_{H_2} = 2p_{O_2}$, and increasing p_{O_2} beyond this point no longer provides benefit over unperturbed thermolysis. (b) Schematic of the tubular redox membrane reactor for splitting of CO_2 and H_2O. CO_2 and H_2O are fed to the inner side of the membrane and dissociate into fuel and O_2, with the latter selectively crossing the membrane into the Ar sweep gas.

sealant (Aremco-Seal 617) were from Kager Industrieprodukte GmbH. CO_2 (99.998%), Ar (99.996%, 99.999%), He (99.999%), and calibration gas mixtures, *i.e.*, 1000 mol ppm H_2 (99.999%) and 500 mol ppm CO (99.997%) in Ar (99.999%), and 1000 mol ppm CO (99.997%), 500 mol ppm CO_2 (99.995%), 500 mol ppm N_2 (99.999%), and 100 mol ppm O_2 (99.999%) in Ar (99.999%) were from Messer Schweiz AG. According to the manufacturer, Ar (99.996%) contained <5 ppm O_2 on a volume basis, equivalent to a limiting $p_{O_2} < 0.5$ Pa.

Membrane fabrication

Capped tubular ceria membranes were produced as reported previously.[12] Briefly, membranes were fabricated using a phase-inversion/sintering method.[30,31] Two polymers, namely PES (5.7 wt%) and PVP (0.5 wt%), were dissolved in NMP (22.0 wt%). Ceria powder (71.8 wt%) was suspended in the polymer solution. The ceria slurry was coated onto membrane templates (highly flexible silicone tubing, 3 mm ID, 7 mm OD, RCT Reichelt Chemietechnik GMbH & Co.), which were placed in a water bath for phase inversion (unfiltered tap water coagulant under ambient conditions). The silicone templates were removed, and the dried membrane precursors were then sintered for 8 hours at 1873 K (oven model HTL 20/17, ThermConcept). The sintered membranes were 6–7 mm OD, 5–6 mm ID, and 150–250 mm in length. Typically, the membrane walls were about 0.5 mm thick. In-depth solid-state characterization of ceria membranes before and after use in the reactor was performed previously.[12] SEM analysis shown in Fig. S1† shows that ceria membranes exposed to both CO_2 and H_2O in thermolysis experiments do not change morphologically, consistent with membranes used in pure-CO_2 experiments.

Experimental setup

The solar membrane reactor system is depicted schematically in Fig. 2. CO_2 and/or H_2O was fed through a feeder tube into the inner side of the membrane while Ar sweep gas was fed into the reactor shell tube in a counter-current flow. This assembly was placed in a thermally insulated solar cavity receiver with an aperture of 4 cm in diameter. A compound parabolic concentrator (CPC) was incorporated into the aperture to boost the solar flux concentration and generate a more uniform directional distribution of concentrated radiation entering the cavity.[32] Experimentation was performed using the high-flux solar simulator (HFSS) of ETH Zurich: an array of seven Xe arcs, close-coupled to truncated ellipsoidal reflectors, provided an external source of intense thermal radiation that closely approximated the heat transfer characteristics of highly concentrating solar energy facilities. The radiative flux distribution at the focal plane was measured optically using a calibrated CCD camera focused on a Lambertian (diffusely reflecting) target. The solar radiative power input to the cavity was calculated by integration of the radiative flux over the aperture area and verified with a water calorimeter. Temperatures were measured at the outer surface of the reactor shell at two heights along the tube (indicated in Fig. 2) using B-type thermocouples. Gas flow rates were regulated using electronic mass flow controllers (MFC, Bronkhorst F-201 C, accuracy 0.5% Rd + 0.1% FS), whereas steam flow was generated using a liquid flow controller (LFC, Bronkhorst Liqui-Flow L23-AAD-33-K-305, accuracy 1% FS) and steam generator (Bronkhorst CEM W-202A-333-K). The product gas composition in each stream was monitored on-line by gas chromatography (GC, Agilent 490 MicroGC).

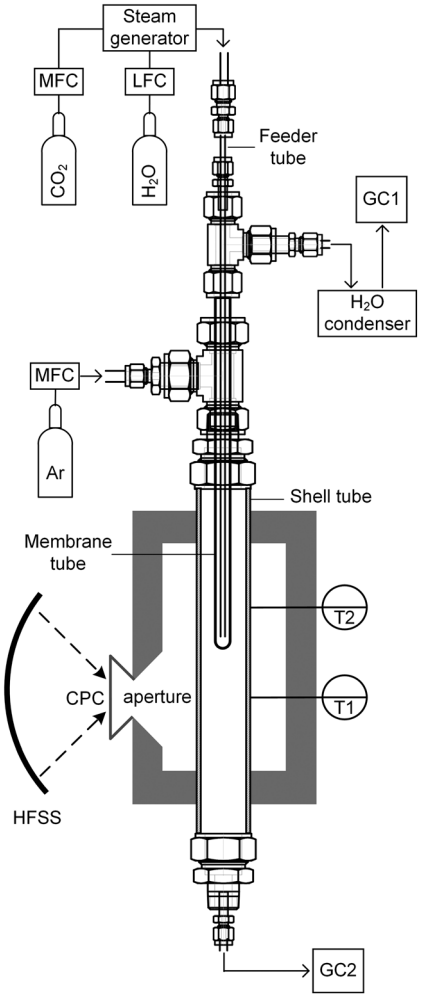

Fig. 2 Schematic and flow diagram of the experimental setup used to test co-thermolysis of CO_2 and H_2O in a membrane reactor. Simulated concentrated solar radiation from the HFSS enters the cavity receiver through the aperture and heats the reactor. Gaseous CO_2 and/or H_2O flows through a feeder tube into the membrane, then flows upward through the annulus between the membrane and feeder tubes before exiting the reactor. The membrane removes O_2 produced from thermolysis. Unreacted H_2O is removed in the condenser and the composition of the remaining gas is analyzed by GC1. In counter-current to the oxidant stream, a sweep gas (Ar) flows through the shell tube, taking up O_2 crossing the membrane, and exits below the cavity receiver to be analyzed by GC2. Not to scale.

Experimental runs

All volumetric flow rates are given under standard conditions (1 bar and 273 K). The HFSS heated the reactor to the desired temperatures in the range of 1723–1873 K with a radiative power input of 2.5–3.0 kW. For water-splitting experiments, steam was fed to the inner side of the membrane at a rate of 104 mL min^{-1} (5 g h^{-1} water to steam generator), carried in by 80–100 mL min^{-1} Ar. For co-feed experiments, the same flow of steam was carried by 75–200 mL min^{-1} CO_2. At the outer side of the membrane, the reactor shell was purged with 200–1000 mL min^{-1} Ar. The compositions of both gas streams exiting the solar reactor were analyzed simultaneously using two gas chromatographs (GC). Steady state was defined as the condition at which the measured gas concentration was within 2% of the mean over the previous five consecutive measurements collected at a frequency of one every two minutes:

$$\frac{\left|c_i(t_n)-\frac{1}{5}\sum_{j=n-5}^{n-1}c_i(t_j)\right|}{\frac{1}{5}\sum_{j=n-5}^{n-1}c_i(t_j)}\leq 0.02 \quad (5)$$

where $c_i(t_j)$ is the volumetric concentration of species i at time point j. Steady-state data were collected for at least 19 minutes and the arithmetic mean was used to summarize the results under each experimental condition.

Thermodynamic analysis

We calculated the thermodynamic equilibrium limits of thermolysis of CO_2 and H_2O in a membrane reactor to compare to experimental results. Relatively fast rates are expected for each reaction step: gas-phase thermolysis, heterogeneous surface reaction, and oxygen bulk diffusion. When each of these serial processes is sufficiently fast, global kinetics are fast, and thermodynamics govern the net reaction. In this case, kinetics can be neglected.

Previous observations with a solar cavity receiver containing a porous ceria structure directly exposed to high-flux irradiation reported that the overall kinetics are not controlled by solid-state diffusion within the crystal lattice.[33] This is also expected for a ceria membrane because the measured values of ambipolar diffusion coefficients of oxygen in ceria (1.5×10^{-5}–4×10^{-4} cm^2 s^{-1} in the range of 1673–1823 K[22]) translate to diffusion times in the order of seconds for the length scales across the 0.5 mm-thick membrane. Thus, as far as solid-state diffusion is concerned, the transport of oxygen vacancies through the membrane is almost instantaneous compared with the time scales of data collection.

Reaction rates have an exponential dependence on temperature, scaling with $\exp(-E_A/RT)$, as seen in the Arrhenius equation. The high temperature in the range of 1723–1873 K and consequent high activity of reactive oxygen vacancies at the surface of the membrane are expected to lead to fast surface exchange of oxygen from the gas into the solid phase.[19] While studies of non-isothermal processes show that the heating rate limits the oxygen release rate, heat transfer should not be limiting in this isothermal process because the heat of the reaction is much lower than the heat input.[23,33] Likewise, the high temperature, along with the catalytic effect of ceria, implies very fast thermolysis reactions in the gas phase.[34] Therefore, a purely thermodynamic model is expected to adequately predict reactor performance.

However, to reach the thermodynamic limit in the countercurrent-flow reactor, there must be a sufficient membrane area and sweep gas flow rate relative to the flow rate of the reactant. To account for the oxygen capacity in a given flow of sweep gas, a thermodynamic model described by Bulfin was applied, which is specific to countercurrent-flow reactors.[35] This approach guarantees compliance with the second law of thermodynamics and conservation of mass along the entire reactor by means of a dimensionless oxygen exchange coordinate, κ, defined as the number of moles of O_2 crossing the membrane up to a certain point along the length, x, per mole of oxidant fed:

$$\kappa(x)=\frac{\int_0^x\left|j_{O_2}(x)\right|dx}{\dot{n}_{oxidant}}, \quad (6)$$

where $\dot{n}_{oxidant}$ is the molar flow rate of H_2O and/or CO_2 $\left(\dot{n}_{CO_2}+\dot{n}_{H_2O}\right)$, and $j_{O_2}(x)$ is the molar flux of O_2 from the oxidant flow to the sweep gas as a function of the length along the membrane. Then p_{O_2} in each flow can be formulated as a function of κ, and $p_{O_2,oxidant}$ is determined by the thermodynamic equilibrium of thermolysis, as described by eqn (3) and (4) in the introduction. For O_2 to spontaneously flow from the oxidant flow to the sweep gas, partial pressures must satisfy $p_{O_2,oxidant}(\kappa) > p_{O_2,sweep}(\kappa)$, and equilibrium is reached if there exists a value of κ in $[0, \kappa_{total}]$ where $p_{O_2,oxidant}(\kappa) = p_{O_2,sweep}(\kappa)$. Bulfin detailed the full methodology in an example tailored to thermolysis in a membrane reactor with a counter-current sweep flow.[35]

The countercurrent-flow thermodynamic model was implemented and solved numerically with Matlab using thermodynamic data from NIST JANAF.[36] The model input parameters are T, p, p_{O_2}, the relative flow of sweep to oxidant ($\dot{n}_{sweep}/\dot{n}_{oxidant}$), and the relative flow rates of CO_2 and H_2O $\left(\dot{n}_{CO_2}/\dot{n}_{H_2O}\right)$. Note that p_{O_2} refers to the O_2 impurity at the inlet of the sweep gas. The values were generally chosen to match experimental conditions as determined from mass flow controller, thermocouple, and GC measurements. For example, the reactor operated at ambient pressure and 1 bar total pressure was set on both sides of the membrane. It was not possible to measure the reaction temperature of the gas inside the membrane. Instead, the measured temperature at the outer wall of the shell tube (certainly greater than the

reaction temperature) and a simple heat transfer model were used to estimate the reaction temperature. Consequently, this analysis presents the thermodynamic limits as a shaded region, where the upper and lower bounds are the limits at the maximum measured shell temperature and the estimated reaction temperature, respectively. In the range of operation, the difference between these temperatures is approximately 50 K. The simple heat transfer model used to calculate this temperature difference is described in the ESI.† The outputs of the thermodynamic model are the partial pressures of the products and conversion of the reactants at equilibrium.

Results and discussion

Fig. 3 summarizes the steady-state specific production rates measured experimentally for fuel, comprising CO (light shading) and H_2 (dark shading), and O_2 as a function of three process variables: (a) time, (b) T, and (c) p_{O_2}. These experiments used a roughly equimolar feed of CO_2 and H_2O and produced fuel with a relatively higher fraction of CO than H_2. This product proportion is consistent with the more favorable change in Gibbs free energy for thermolysis of CO_2 at high temperatures, as seen in Fig. 1a. The average molar ratio O_2 : fuel over 19 experiments was 0.53 ± 0.07, corroborating a closed mass balance. Furthermore, no other by-products were detected, indicating the absence of undesired side reactions. Specifically, Fig. 3a shows production rates over time at steady state at a nominal T of 1873 K and p_{O_2} of 0.4 Pa. Note that T refers to the maximum measured shell temperature and p_{O_2} refers to the partial pressure of O_2 at the Ar inlet, which is the minimum p_{O_2} in the system and determined by the impurity in the sweep gas. Gas evolution rates leveled off at a constant incident radiative flux of about 3500 suns (1 sun = 1 kW m^{-2}) over the cavity's aperture, and thus the reactor demonstrated continuous, steady-state operation under isothermal conditions. Fig. 3b shows the steady-state average production rates as a function of T in the range of 1723–1873 K. Mass flow rates were kept constant at 5 g h^{-1} H_2O with 100 mL min^{-1} CO_2 to the inner side and 500 mL min^{-1} Ar to the outer side of the membrane (L denotes standard liters). The measured p_{O_2} ranged from 0.4–1.7 Pa due to variation in the small amount of air leakage into the reactor during different experimental runs. The specific fuel and O_2 production rates at steady state increased with temperature, in accordance with the thermodynamic dependence on $\exp(-\Delta G^\circ/RT)$. Finally, Fig. 3c shows the steady-state average production rates as a function of p_{O_2} in the range of 0.2–0.9 Pa at 1873 K. Although the range of p_{O_2} tested was small, the gas production rates indeed decreased at higher p_{O_2}, as expected from the equilibrium relationship for the thermolysis of CO_2 and H_2O described in eqn (3) and (4). However, to achieve this range of p_{O_2}, the flow rate of Ar was adjusted, thus changing the relative flow of sweep gas, $\dot{n}_{sweep}/\dot{n}_{oxidant}$, which is also a key thermodynamic parameter in this reactor system.

Fig. 4 shows the experimental steady-state conversion of CO_2 to CO and H_2O to H_2 as a function of (a) T in the range of 1723–1873 K at p_{O_2} = 1 Pa, $\dot{n}_{sweep}/\dot{n}_{oxidant}$ = 2.4, and (b) $\dot{n}_{sweep}/\dot{n}_{oxidant}$ ranging from 1–5 at T = 1873 K, p_{O_2} = 0.5 Pa. The thermodynamic limits are also indicated, denoted by a band whose upper and lower bounds are calculated as described above at T_{shell} and the estimated reaction temperature, T_{shell} − 50 K, respectively. The band is wider for CO_2 than that for H_2O because its reaction favorability changes more steeply with T. Like the gas production rates, the conversion of reactants shown in Fig. 4a increased with T, as expected. The conversion also increased at higher relative sweep rates shown in Fig. 4b, because $\dot{n}_{sweep}/\dot{n}_{oxidant}$ determines the total amount of O_2 that can be removed across the membrane at equilibrium. In fact, the thermodynamic analysis reveals that the trend in production rates observed in Fig. 3c is more attributable to varying $\dot{n}_{sweep}/\dot{n}_{oxidant}$ than p_{O_2}. The p_{O_2} in the sweep gas must be lower than p_{O_2} in the oxidant stream at all points along the membrane to drive transfer of O_2. At sufficiently low p_{O_2}, however, this parameter does not have a strong influence on the conversion of reactants, shown in Fig. S3 in the ESI.† In the range of p_{O_2} observed in the experiments (0.2–0.9 Pa), the theoretical conversion of each reactant at constant $\dot{n}_{sweep}/\dot{n}_{oxidant}$ is almost flat, while the experimental data points exhibit a trend due to varying relative sweep rates. In contrast, the same experimental data plotted against $\dot{n}_{sweep}/\dot{n}_{oxidant}$ shown in Fig. 4b match the shape of the equilibrium limit curves.

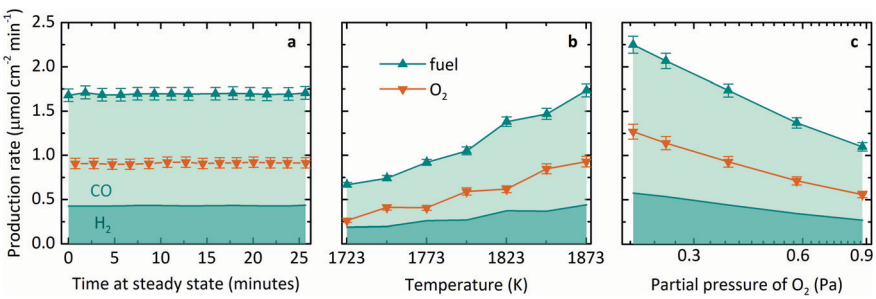

Fig. 3 Trends in steady-state specific gas production rates. Feed was equimolar CO_2 and H_2O in all cases. Fuel production is composed of two contributions distinguished by shades: CO (light) and H_2 (dark). (a) Steady-state production rates of fuel (CO and H_2) and O_2 *vs.* time at 1873 K and 0.4 Pa O_2; (b) steady-state average production rates of fuel and O_2 *vs.* T, keeping all mass flow rates constant; (c) steady-state average production rates of fuel and O_2 *vs.* p_{O_2}, keeping T constant at 1873 K.

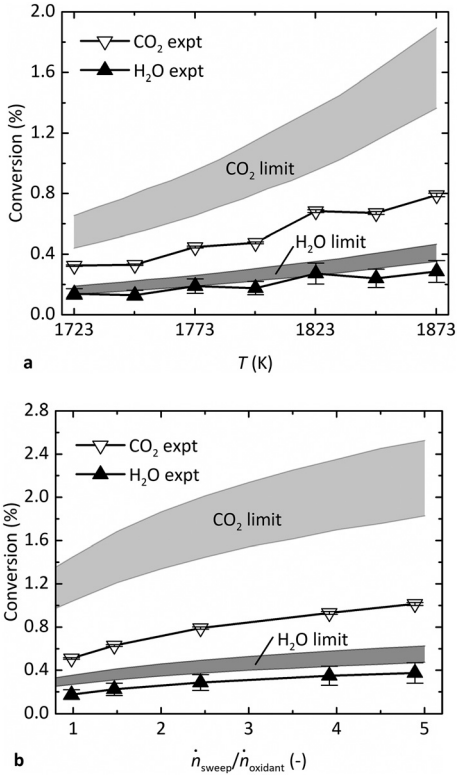

Fig. 4 Comparison of the average experimental conversion of CO_2 and H_2O at steady state *versus* equilibrium limits as a function of (a) T, at $\dot{n}_{sweep}/\dot{n}_{oxidant}$ = 2.4 and 1 Pa O_2, and (b) $\dot{n}_{sweep}/\dot{n}_{oxidant}$, at 1873 K and 0.5 Pa O_2.

In general, the results indicate that the reactor performance indeed approaches the thermodynamic limit for a countercurrent flow reactor. Importantly, the experimental conversion does not exceed the theoretical limit. Furthermore, the experimental points lie closer to the lower bound of the equilibrium region, suggesting that the simple heat transfer model is necessary and effective to estimate the reaction temperature. While the experimental conversion of H_2O closely follows the lower bound of the predicted thermodynamic limit, the experimental conversion of CO_2 falls short. The discrepancy is less than a factor of two and may be a result of the water–gas shift (WGS) reaction occurring at lower T downstream of the reactor, before the GC analysis. The WGS consumes some CO to produce additional H_2 and is thus the difference of the CO_2 and H_2O dissociation reactions (eqn (2) minus eqn (1)):

$$CO + H_2O \leftrightarrow H_2 + CO_2 \quad (7)$$

In this case, the GC measurements may not be representative of the composition in the reactor; the actual conversion of CO_2 may have been higher, and the conversion of H_2O lower, potentially equalizing the difference seen in Fig. 4 between the experimental data and the limit for each gas.

Fig. 5 illustrates the effect of the molar feed ratio, CO_2:H_2O, on the: (a) steady-state average production rates of fuel and O_2, (b) conversions of CO_2 and H_2O, and (c) molar ratio of the two fuels produced, CO:H_2. Fig. 5b and c show the comparison of the results measured experimentally with those predicted from thermodynamics. The relative flow rates of CO_2 and H_2O were varied while maintaining the steam feed rate at 5 g h^{-1} H_2O, temperature at 1873 K, and p_{O_2} at 0.5 Pa. Fig. 5a shows that the overall fuel production (sum of H_2 and CO) increased with CO_2:H_2O, as did the production rate of CO, which occurred because the total feed rate and CO_2 feed rate both increased. The production rate of H_2, on the other hand, decreased with CO_2:H_2O. It must be emphasized that $\dot{n}_{sweep}/\dot{n}_{oxidant}$ did not remain constant over experimentation, but rather decreased with CO_2:H_2O because the flow rate of sweep gas remained constant. A constant flow rate of sweep gas is less effective at maintaining low p_{O_2} as the amount of O_2 to be removed increases. In the case of CO, the effect of increasing CO_2 feed rate compensated for the

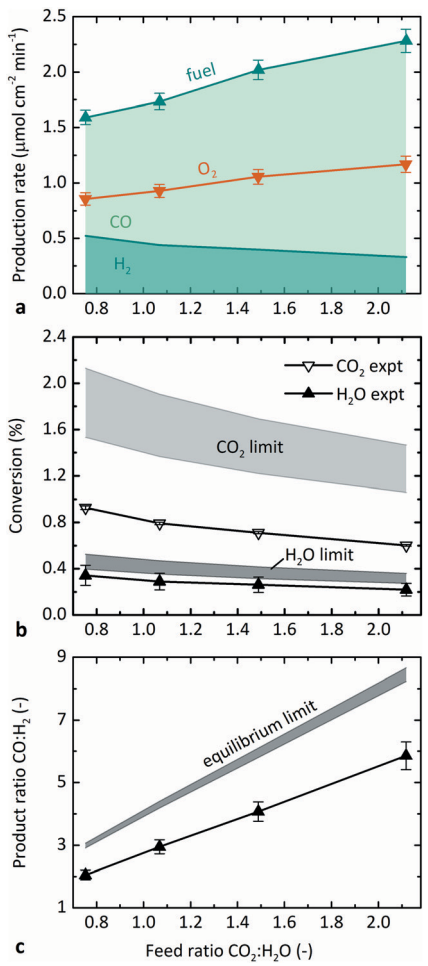

Fig. 5 Effect of molar feed ratio CO_2:H_2O on: (a) steady-state average production rate of fuel and O_2, where fuel is composed of two contributions distinguished by shades: CO (light) and H_2 (dark); (b) molar conversion of CO_2 and H_2O calculated from experiments and their limits at equilibrium; and (c) molar fuel ratio CO:H_2 measured experimentally and at equilibrium. Reaction conditions were $\dot{n}_{sweep}/\dot{n}_{oxidant}$ varying from 1.6–2.5,constant 5 g h^{-1} H_2O feed rate, 1873 K, and 0.5 Pa O_2.

decreasing sweep ratio, so that the net production rate increased. However, the H_2 production decreased.

The confounding factors of changing both the total feed rate and the relative sweep rate are accounted for by plotting conversion instead of the production rate in Fig. 5b. As seen in Fig. 4, the absolute values of H_2O conversion in Fig. 5b again match the model results better than those for CO_2. The experimental conversions of both CO_2 and H_2O decreased slightly with increasing $CO_2:H_2O$, in agreement with the trend predicted at equilibrium. There are two contributions to the negative trend in conversion. First, as already mentioned, $\dot{n}_{sweep}/\dot{n}_{oxidant}$ decreased with $CO_2:H_2O$, which decreased the conversion. However, the conversion of each reactant is predicted to decrease slightly with $CO_2:H_2O$ even with a constant $\dot{n}_{sweep}/\dot{n}_{oxidant}$. The second reason for the trend is related to the difference in favorability of thermolysis of CO_2 and H_2O. As the feed ratio increases, a higher proportion of the feed is CO_2, which has a higher conversion than H_2O under these conditions. In fact, the overall conversion of reactants to products actually increased slightly with increasing $CO_2:H_2O$. However, the O_2 capacity of the sweep gas was unchanged and therefore the conversion of each individual reactant must decrease to balance the production of O_2 with its removal. This result indicates that a feed of CO_2 requires a higher relative sweep rate than an equal feed of H_2O, because its higher potential conversion leads to a larger amount of O_2 that must be removed.

Consistent with Fig. 5a, Fig. 5c shows that the product ratio $CO:H_2$ increased with increasing feed ratio $CO_2:H_2O$, as expected intuitively. Interestingly, $CO:H_2$ is always greater than the corresponding $CO_2:H_2O$, which further confirms that dissociation of CO_2 is more favorable than that of H_2O under equivalent conditions. The observed experimental trend qualitatively matches equilibrium thermodynamics, though with a smaller slope, because the experimental conversion of CO_2 is lower than predicted. In consideration of downstream processing, the Fischer–Tropsch synthesis favors a syngas feed with 1 : 2 moles $CO:H_2$.[37,38] According to Fig. 5c, the product ratio can be adjusted *via* the feed ratio, and a 1 : 2 product ratio would require a feed ratio smaller than the minimum tested here.

The maximum conversions observed experimentally were 1.0% CO_2 and 0.4% H_2O at 1873 K, $\dot{n}_{sweep}/\dot{n}_{oxidant}$ = 5, and 0.2 Pa O_2 (0.7% overall conversion of reactants). In general, the absolute values of both theoretical and experimental conversion were lower in the co-feed case tested here than in the pure-CO_2 feed case tested previously,[12] because the relative sweep rates were lower in this set of experiments. The base case $\dot{n}_{sweep}/\dot{n}_{oxidant}$ was 8 in pure-CO_2 experiments and 2.4 in these co-feed experiments. The relative sweep rate is a significant parameter for sweep gas operation, and the application of the countercurrent flow model was essential to accurately predict the behavior of the reactor. Furthermore, although there was no effort to optimize the efficiency of the reactor in these proof-of-concept experiments, $\dot{n}_{sweep}/\dot{n}_{oxidant}$ also impacts efficiency because it determines how much sweep gas must be heated and circulated per unit fuel produced.

Conclusion

We have demonstrated steady-state splitting of a mixed feed containing CO_2 and H_2O into separate streams of syngas fuel and O_2 using an isothermal tubular ceria membrane reactor driven by simulated concentrated solar radiation. The experimental results generally agreed with trends predicted by thermodynamics. The conversion of CO_2 to CO was favored over H_2O to H_2, consistent with the energetics of the respective thermolysis reactions. The co-thermolysis of a mixture of CO_2 and H_2O is more complex than feeding either CO_2 or H_2O separately to the reactor, both experimentally and in the theoretical analysis. In the co-feed case, the mixture of CO_2, H_2O, CO, and H_2 could undergo additional reactions, especially the reverse water–gas shift (RWGS). As seen in eqn (7), the WGS reaction is not independent of the two thermolysis reactions, and thus does not change the equilibrium conversion of each reactant from the pure-feed values. Other possible reactions were found to be negligible from the lack of by-products predicted by thermodynamics and measured experimentally under these conditions. The absence of by-products and a 2 : 1 ratio of fuel : oxygen together confirmed 100% selectivity for the desired splitting reactions.

The solar thermochemical membrane reactor unifies both CO_2 and H_2O splitting in a single modular and scalable device and offers a technically viable pathway to single-step syngas production. However, determining an appropriate relative sweep rate is challenging in co-feed operation because the different favorability for thermolysis of CO_2 and H_2O implies different optimums for each species. In addition, these energetic differences mean that H_2O needs to be fed in large excess to achieve a desirable syngas composition. Therefore, it may still be attractive to produce CO and H_2 separately and mix them into syngas as needed. Furthermore, the single-step approach incorporated in the membrane reactor must compete with multistep cycles currently available. Thus, further R&D and alternative membrane configurations are needed to boost mass conversions and consequently reach favorable solar-to-fuel energy efficiencies, a challenge because T and p_{O_2} determine the thermodynamic limits.

Conflicts of interest

There are no conflicts to declare.

Acknowledgements

This work was funded by the Swiss National Science Foundation (Ambizione Energy Grant No. 166883) and by the Chinese Academy of Sciences (International Collaboration Key Program award no. 182211KYSB20160043). We thank Brendan Bulfin for fruitful discussions and Patrick Basler and Simon Minder for supporting the experimental campaign.

References

1 N. S. Lewis, *Science*, 2016, **351**, aad1920.

2 G. A. Ozin, *Adv. Mater.*, 2015, **27**, 1957–1963.
3 J. A. Herron, J. Kim, A. A. Upadhye, G. W. Huber and C. T. Maravelias, *Energy Environ. Sci.*, 2015, **8**, 126–157.
4 D. Marxer, P. Furler, J. Scheffe, H. Geerlings, C. Falter, V. Batteiger, A. Sizmann and A. Steinfeld, *Energy Fuels*, 2015, **29**, 3241–3250.
5 W. C. Chueh, C. Falter, M. Abbott, D. Scipio, P. Furler, S. M. Haile and A. Steinfeld, *Science*, 2010, **330**, 1797–1801.
6 M. Romero and A. Steinfeld, *Energy Environ. Sci.*, 2012, **5**, 9234.
7 Y. Hao, C. K. Yang and S. M. Haile, *Phys. Chem. Chem. Phys.*, 2013, **15**, 17084–17092.
8 C. L. Muhich, B. W. Evanko, K. C. Weston, P. Lichty, X. Liang, J. Martinek, C. B. Musgrave and A. W. Weimer, *Science*, 2013, **341**, 540–542.
9 L. J. Venstrom, R. M. De Smith, Y. Hao, S. M. Haile and J. H. Davidson, *Energy Fuels*, 2014, **28**, 2732–2742.
10 E. A. Fletcher and R. L. Moen, *Science*, 1977, **197**, 1050–1056.
11 J. E. Noring, R. B. Diver and E. A. Fletcher, *Energy*, 1981, **6**, 109–121.
12 M. Tou, R. Michalsky and A. Steinfeld, *Joule*, 2017, **1**, 146–154.
13 A. Evdou, L. Nalbandian and V. Zaspalis, *J. Membr. Sci.*, 2008, **325**, 704–711.
14 W. Jin, C. Zhang, X. Chang, Y. Fan, W. Xing and N. Xu, *Environ. Sci. Technol.*, 2008, **42**, 3064–3068.
15 L. Nalbandian, A. Evdou and V. Zaspalis, *Int. J. Hydrogen Energy*, 2009, **34**, 7162–7172.
16 H. Wang, Y. Hao and H. Kong, *Int. J. Energy Res.*, 2015, **39**, 1790–1799.
17 X. Y. Wu, L. Chang, M. Uddi, P. Kirchen and A. F. Ghoniem, *Phys. Chem. Chem. Phys.*, 2015, **17**, 10093–10107.
18 L. Zhu, Y. Lu and S. Shen, *Energy*, 2016, **104**, 53–63.
19 T. C. Davenport, C.-K. Yang, C. J. Kucharczyk, M. J. Ignatowich and S. M. Haile, *Energy Technol.*, 2016, **4**, 764–770.
20 P. Furler, J. R. Scheffe and A. Steinfeld, *Energy Environ. Sci.*, 2012, **5**, 6098–6103.
21 P. M. Geffroy, J. Fouletier, N. Richet and T. Chartier, *Chem. Eng. Sci.*, 2013, **87**, 408–433.
22 S. Ackermann, J. R. Scheffe and A. Steinfeld, *J. Phys. Chem. C*, 2014, **118**, 5216–5225.
23 W. C. Chueh and S. M. Haile, *Philos. Trans. R. Soc., A*, 2010, **368**, 3269–3294.
24 M. Mogensen, N. M. Sammes and G. A. Tompsett, *Solid State Ionics*, 2000, **129**, 63–94.
25 A. Glück, R. Tamme, H. Kalfa and C. Streuber, *Sol. Energy Mater.*, 1991, **24**, 240–248.
26 R. Bader, L. J. Venstrom, J. H. Davidson and W. Lipiński, *Energy Fuels*, 2013, **27**, 5533–5544.
27 S. Brendelberger, H. von Storch, B. Bulfin and C. Sattler, *Sol. Energy*, 2017, **141**, 91–102.
28 M. Ezbiri, K. M. Allen, M. E. Galvez, R. Michalsky and A. Steinfeld, *ChemSusChem*, 2015, **8**, 1966–1971.
29 B. Bulfin, J. Vieten, C. Agrafiotis, M. Roeb and C. Sattler, *J. Mater. Chem. A*, 2017, **5**, 18951–18966.
30 W. He, H. Huang, J.-F. Gao, L. Winnubst and C.-S. Chen, *J. Membr. Sci.*, 2014, **452**, 294–299.
31 X. Tan, Y. Liu and K. Li, *Ind. Eng. Chem. Res.*, 2005, **44**, 61–66.
32 W. T. Welford and R. Winston, *High Collection Nonimaging Optics*, Academic Press, Inc., San Diego, 1989.
33 P. Furler, J. Scheffe, M. Gorbar, L. Moes, U. Vogt and A. Steinfeld, *Energy Fuels*, 2012, **26**, 7051–7059.
34 Q. Jiang, Z. Chen, J. Tong, M. Yang, Z. Jiang and C. Li, *Chem. Commun.*, 2017, **53**, 1188–1191.
35 B. Bulfin, *Phys. Chem. Chem. Phys.*, 2019, **21**, 2186–2195.
36 M. W. Chase, C. A. Davies, J. R. Downey, D. J. Frurip, R. A. McDonald and A. N. Syverud, *NIST-JANAF Thermochemical Tables: NIST Standard Reference Database 13*, Standard Reference Data Program, National Institute of Standards and Technology, 1998, DOI: 10.18434/T42S31.
37 H. Schulz, *Appl. Catal., A*, 1999, **186**, 3–12.
38 D. Leckel, *Energy Fuels*, 2009, **23**, 2342–2358.